Supplementary Information

High-resolution patterning of reusable membranes for spatially predesigned single-walled carbon nanotube films for advanced optical and sensing applications

Nikita I. Raginov[1], Arina V. Radivon[2,3,4], Svetlana I. Serebrennikova[1], Nikita E. Gordeev[1], Aliya R. Vildanova[1], Hassaan A. Butt[1], Boris S. Voloskov[1], Ignat I. Rakov[1], Igor E. Spector[3,], Aleksey V. Chernykh[5], Elizaveta Tsiplakova[5], Sergey A. Gusev[1], Alexander A. Safonov[1], Li Li[6], Hao Tian[6], Nikolay V. Petrov[5,6], Maria G. Burdanova[2,3], Dmitry V. Krasnikov[1,*], Albert G. Nasibulin[1,*]

[1] Skolkovo Institute of Science and Technology, Moscow, 121205, Russia

[2] Center for Photonics and 2D Materials, Moscow Institute of Physics and Technology, Dolgoprudny 141701, Russia

[3] Prokhorov General Physics Institute of the Russian Academy of Sciences, Moscow 119991, Russia

[4] Institute of Solid State Physics of the Russian Academy of Sciences, Chernogolovka 142432, Russia

[5] ITMO University, St. Petersburg 191002, Russia

[6] School of Physics, Harbin Institute of Technology, 150001, Harbin, China

Corresponding author's email: a.nasibulin@skol.tech, d.krasnikov@skol.tech

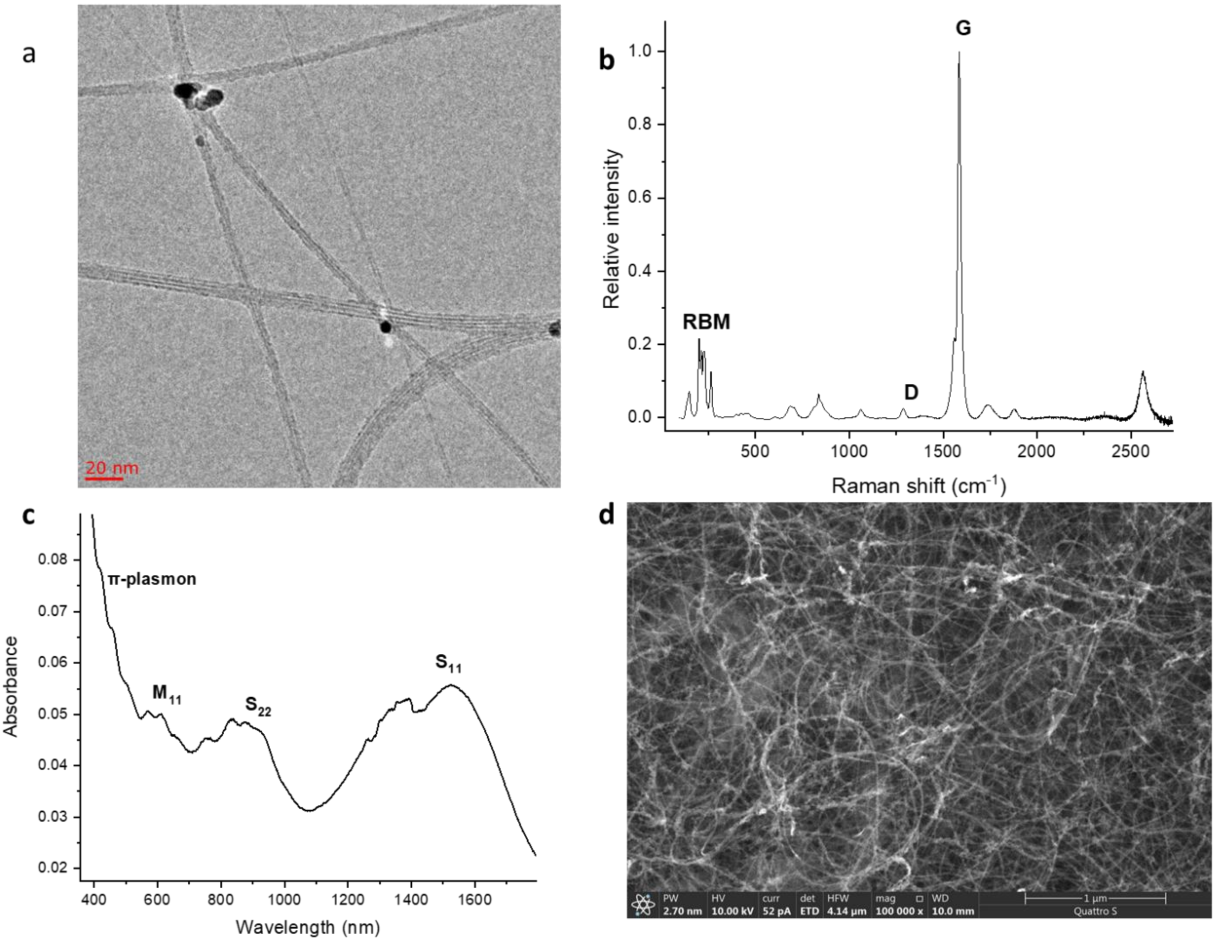

Figure S1. SWCNT characterization: a) TEM image, b) Raman spectrum, c) Absorbance graph of SWCNT film obtained with UV-vis-NIR spectrometry, d) SEM image of SWCNT film dry-transferred to silicon substrate.

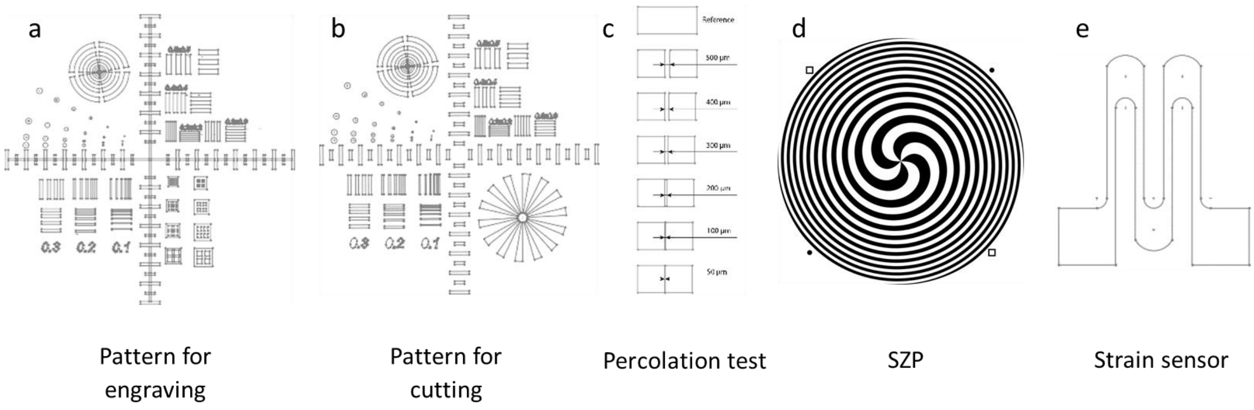

Figure S2. Pattern designs: a) Resolution test for stencil-free approach of patterning. b) Resolution test for stencil-supported patterning approach c) Percolation test of square pairs with different gap to analyze efficiency of blocking aerosol flow paths through membrane, d) Four-charged spiral zone plate pattern for fabrication of THz range tunable optical device, e) Strain sensor for assessment of material deformation under force applied.

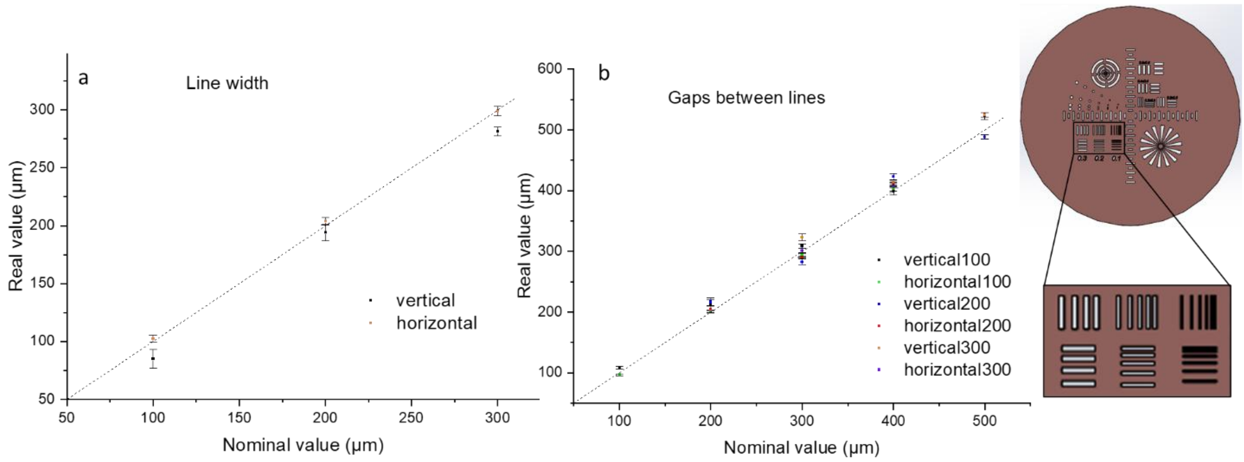

Figure S3. Resolution test of mask, fabricated with laser cutting through copper foil, for stencil-supported imprinting approach. Dimensions of elements were investigated using optical microscopy, and deviations from initially designed pattern were assessed. For test object line / space elements were chosen; to verify absence of dependence on direction of laser movement, test pattern was duplicated perpendicular to the origin one. a) Comparison of element width on stencil and initial predetermined dimensions for lines 100, 200 and 300 µm. b) Comparison of distance between elements predetermined in drawing and on stencil.

Fabricated mask for stencil-supported imprinting was examined on reproduction quality of initial design predetermined in drawing. Due to resolution limits of laser used for cutting, line widths on stencil are narrower comparing with original design and gaps between elements are wider. Average deviation from nominal value is around 10 µm without any difference for different element dimensions and their orientation.

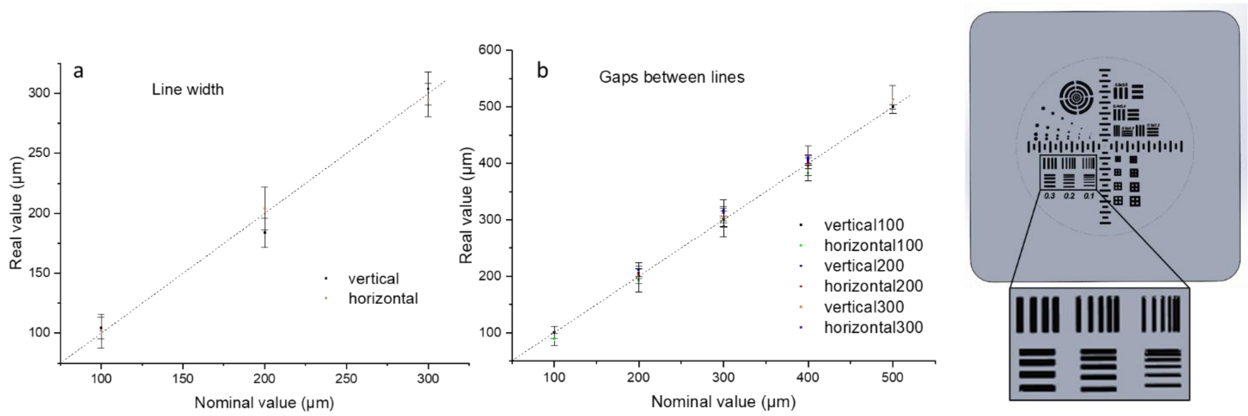

Figure S4. Resolution test of mask, fabricated with laser engraving on stainless steel substrate, for stencil-free imprinting approach. Dimensions of elements were investigated using optical microscopy, and deviations from initially designed pattern were assessed. For test object line / space elements were chosen; to verify absence of dependence on direction of laser movement, test pattern was duplicated perpendicular to the origin one. a) Comparison of element width on stencil and initial predetermined dimensions for lines 100, 200 and 300 μm. b) Comparison of distance between elements predetermined in drawing and on stencil.

Fabricated mask for stencil-free imprinting was examined on reproduction quality of initial design predetermined in drawing. Dimensions of elements on stencil are close to original design with average deviation of 5 μm. However, due to multiple engravings to achieve sufficient depth for imprinting, element borders are rougher comparing with mask prepared for stencil-supported approach.

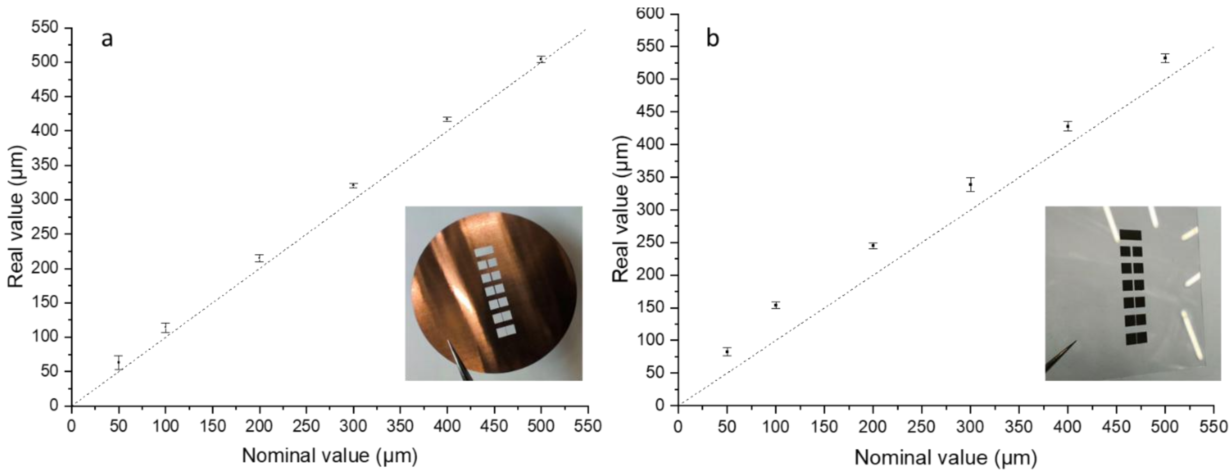

Figure S5. Analysis of percolation test pattern: a) Comparison of gap size between elements on stencil and predetermined in drawing. b) Comparison of gap size between elements of collected SWCNT film and predetermined dimensions in drawing.

Nominal gap size, μm	50	100	200	300	400	500
Gaps on stencil, μm	63 ± 10	114 ± 7	214 ± 5	320 ± 3	416 ± 3	504 ± 5
Gaps in SWCNT film, μm	82 ± 6	153 ± 5	244 ± 4	338 ± 10	428 ± 7	532 ± 6

Table S1. Comparison of nominal gap values and obtained gap size for stencil and SWCNT film.

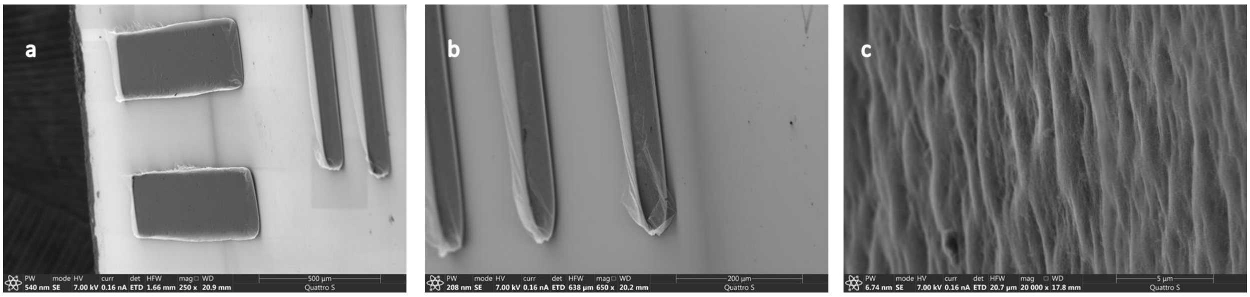

Figure S6. SEM images captured at 45° tilt angle of patterned SWCNT film dry transferred onto silicon substrate. a-b) Images of patterned SWCNT film collected with stencil-supported membrane. Region of resolution test pattern with line / space gratings was captured. c) Surface of patterned SWCNT film

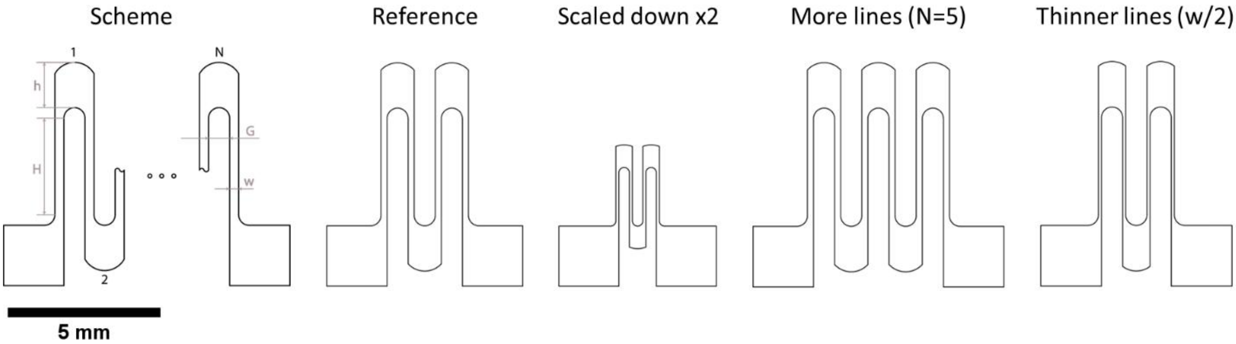

Figure S7. Scheme of strain sensor design and patterns used for test. H is the length of the line, w is the line width, G is the gap width between lines, h is the height of the bridge between lines, and N is the number of loops.

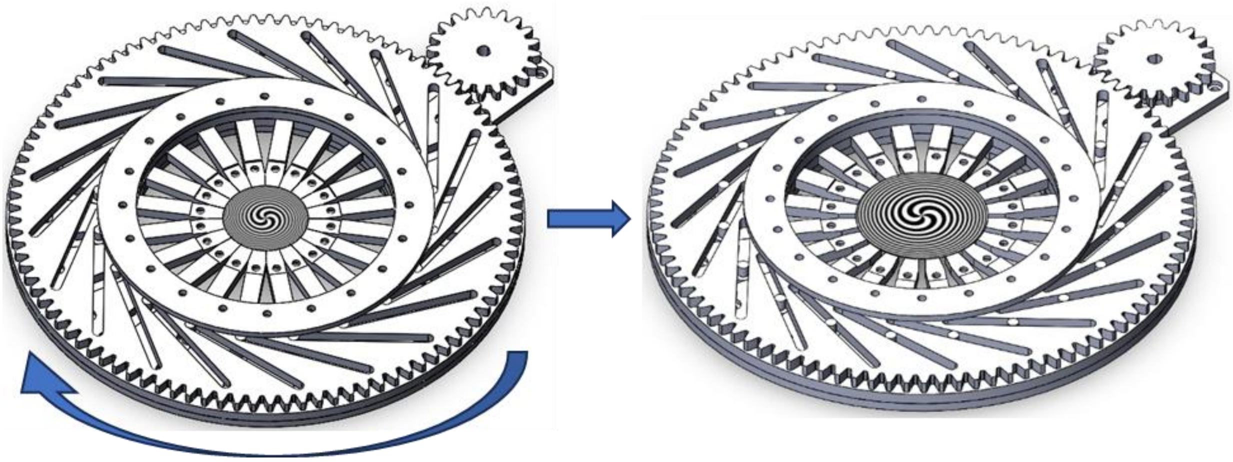

Figure S8. A Scheme for a radial stretching machine. Principle of the mechanism of this device is similar to the iris diaphragm. The small gear actuated by stepper motor twists big gear with grooves for slider pins. Twenty sliders each are placed in individual slot under big gear. With rotation of the big gear pins shift and sliders move along their slots. Patterned SWCNT film of four-charged spiral zone plate on a flexible substrate is attached to the ends of sliders in the center of stretching device. Symmetric movement of sliders allows to uniformly stretch flexible substrate and change scale of patterned film.

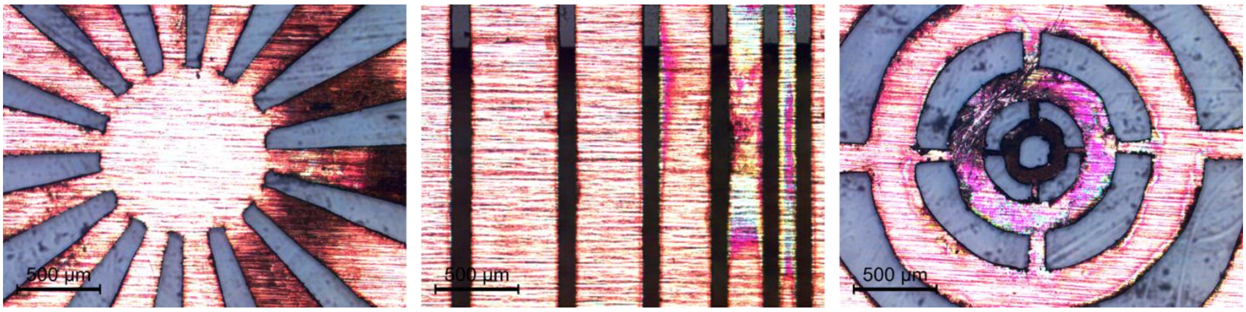

Figure S9. Optical microscopy photos of copper stencil prepared for patterning resolution test. Examples of elements cut through copper foil for stencil-supported imprinting approach.

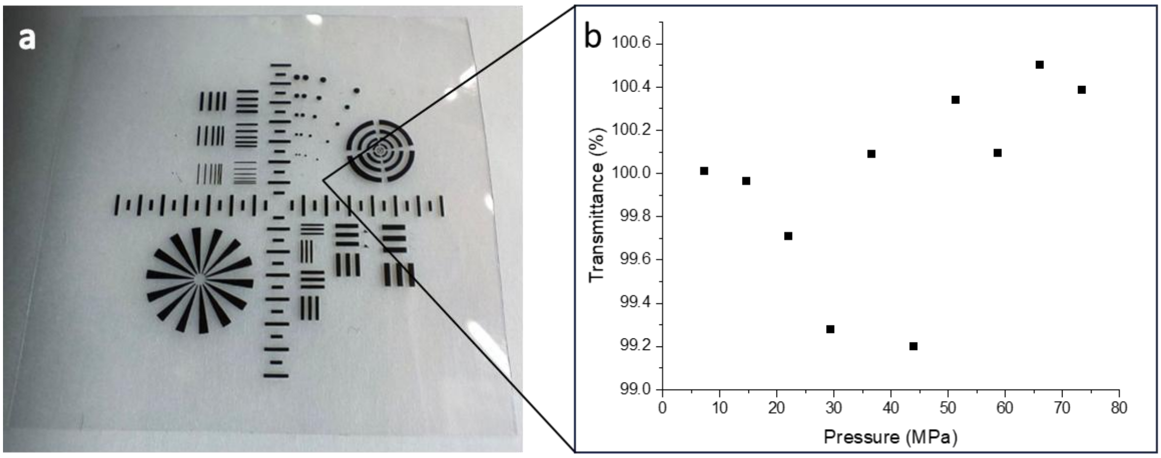

Figure S10. a) Photo of a patterned SWCNT film dry transferred onto PET substrate for resolution test of stencil-supported imprinting approach. b) Dependence of transmittance on imprinting pressure value for areas between patterned SWCNT film elements. The apparent transmittance is related to the PET substrate (thickness variation, reflectance).

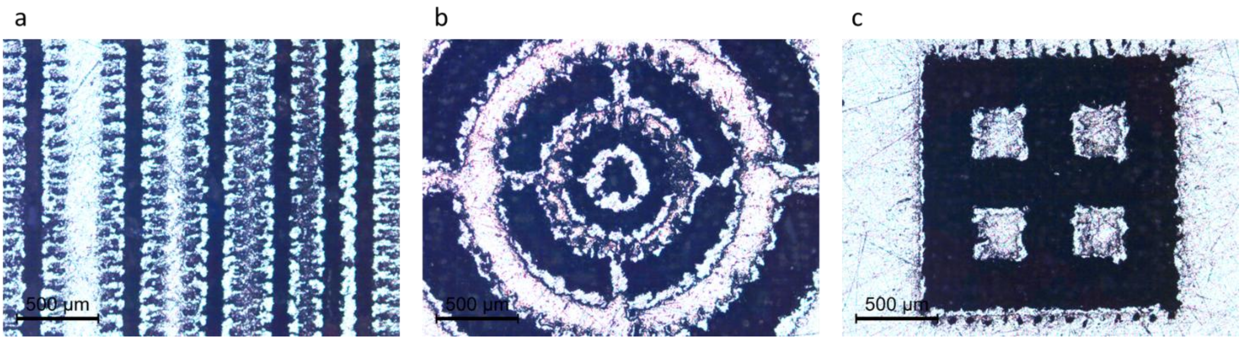

Figure S11. Optical microscopy photos of stainless-steel stencil prepared for patterning resolution test. Examples of elements engraved for stencil-free imprinting approach.

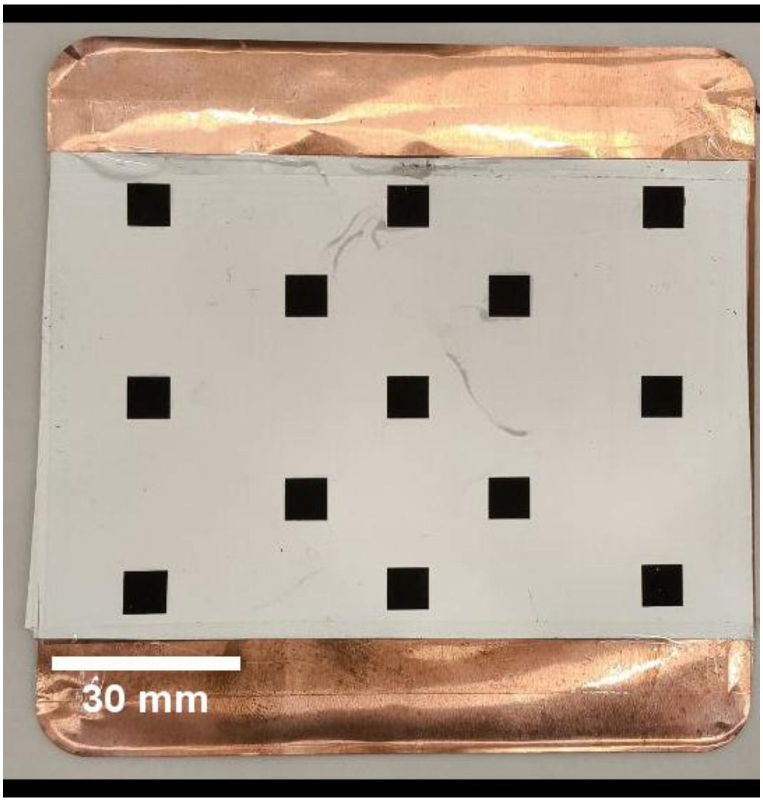

Figure S12. Patterned SWCNT film on 8x10 cm^2 modified membrane.

1. Mechanical tests

For the first type of test, the sensor was attached to the same substrate used for tensile strain characterization (for continuity of findings). Testing was conducted on an Instron 5969 universal testing machine. An R=0.1 (tension-tension cycle) was used since the substrate is brittle and does not withstand compressional force in such characterization. A UTS of 10% was used as the upper stress limit (5 MPa), whereas a 1% UTS was used as the lower stress limit (0.5 MPa). The characterization was conducted in a strain-controlled mode with a 5 MPa stress limit. The sensor was tested for 3000 cycles continuously, and a combined dynamic loading-static hold cycle was used to ensure proper durability and sensing degradation identification. A cross-head speed of 2mm/min was used for the loading and unloading portions of the cycles, whereas the relaxation (time between mechanical loading) and mechanically loaded (static loading at 5 MPa) portions of the cycles lasted 1 second each. The results from the initial ~1000 cycles are shown in Figure S13 (a) and (b), whereas the first 100 seconds of the test (for ease of viewing artefacts) are shown in (c) and (d).

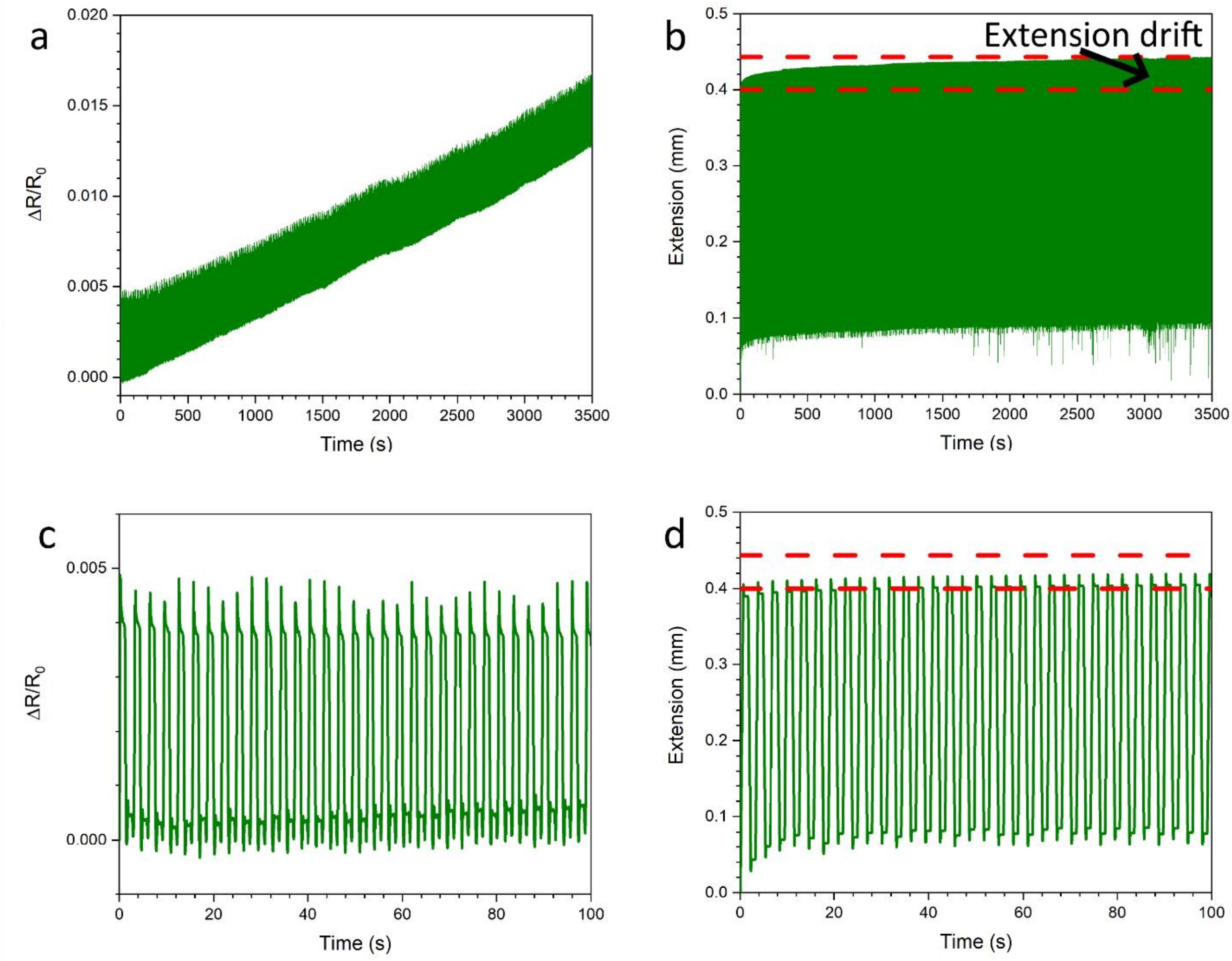

Figure S13: The a) piezoresistive and b) extension-time responses of the sensor and substrate, respectively. c) shows the magnified piezoresistive response cycles, whereas d) shows the mechanical response cycles for the first 100 seconds. The lower red dotted line indicates the initial baseline extension, whereas the upper indicates the final measured extension after ~1000 cycles.

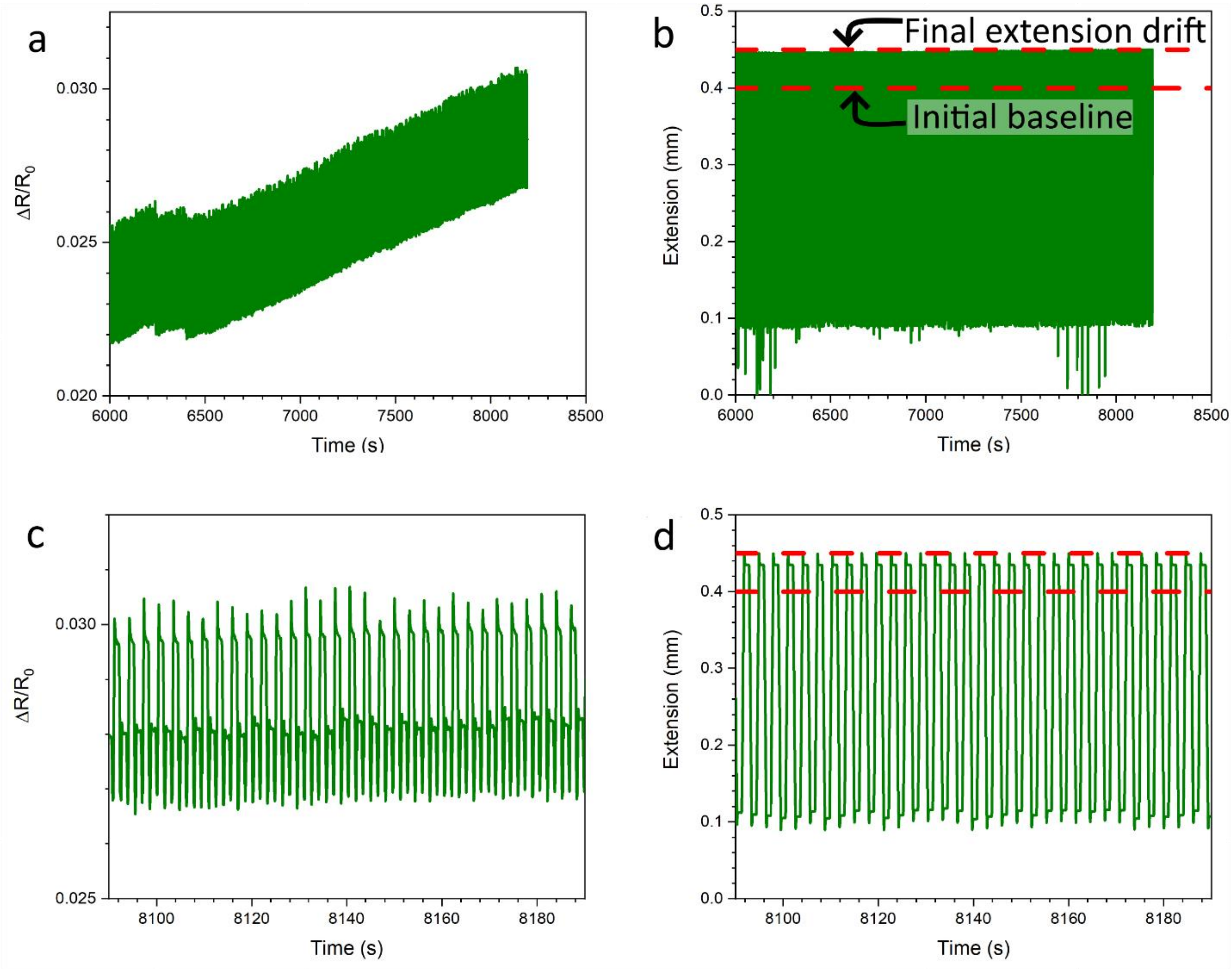

Figure S14: The a) piezoresistive and b) extension-time responses of the sensor and substrate, respectively. c) shows the magnified piezoresistive response cycles, whereas d) shows the mechanical response cycles for the last 100 seconds. The lower red dotted line indicates the initial baseline extension, whereas the upper indicates the final measured extension after 3000 cycles.

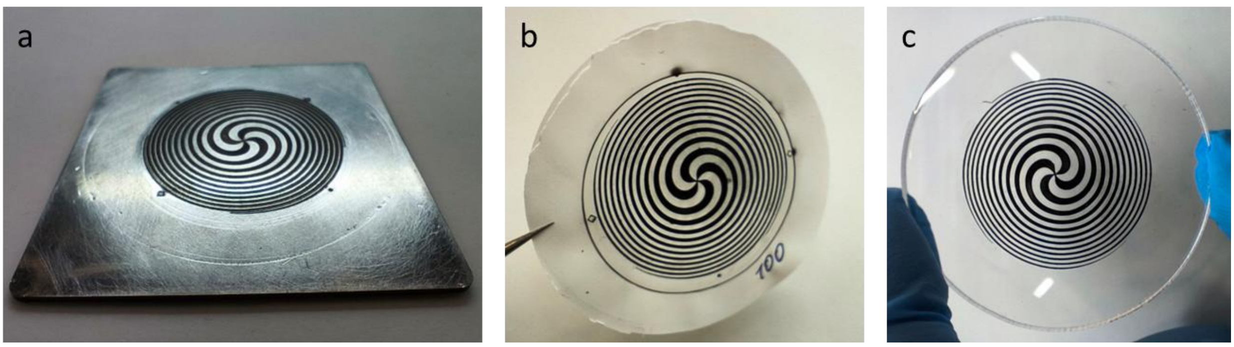

Figure S15. a) Photo of an engraved pattern of four-charged spiral zone plate prepared on stainless-steel plate. b) Photo of a patterned SWCNT film collected on imprinted nitrocellulose filter. c) Photo of a patterned SWCNT film of SZP design was dry-transferred onto polymer glass substrate.

2. Analysis of focal-plane intensity behavior under SZP stretching

To interpret the experimentally observed rotation of intensity spots in the focal plane area during stretching of the SZP (Figure 6, main manuscript), it is necessary to understand whether this rotation is related to the physical rotation of the elements of the spiral structure of the diffraction optical element itself or is due to other effects, such as a change in focal length. This section is devoted to the analysis of this issue by comparing the geometry of the SZP during the stretching and the results of numerical modeling.

2.1. Analysis of the effect of SZP stretching on the position of the SZP stripes

Figure S16 shows a set of pairs of overlapped SZP patterns: unstretched one (0%) and 4% (a), 8% (b) and 12% (c) respectively. Stretched patterns are displayed semi-transparently. The overlay reveals an azimuthal shift in the positions of the stripes, even though the SZP is subjected to a purely radial stretch. A slight rotation of the stripes, which gradually increases with both radial coordinate and the degree of stretching, is evident from the center of the images. This is visualized by the gray areas resulting from the translucent overlay of one SZP on the other. This rotation additionally leads to the heterogeneous variation (along the radial direction) of the positions of the stripes that form the spiral structure, depending on the degree of stretching. For example, with a stretching degree of 12% (see Figure S16c), a significant rotation of the lines containing SWCNT is observed in two annular regions at a certain radial distance (they appear gray in the image due to overlap), while there are no significant changes in the center and periphery of the SZP. This relationship is expected to hold both under experimental conditions and in the numerical simulations. Because of the latter it cannot explain the rotation of intensity spots observed in the experiment during stretching of the SZP.

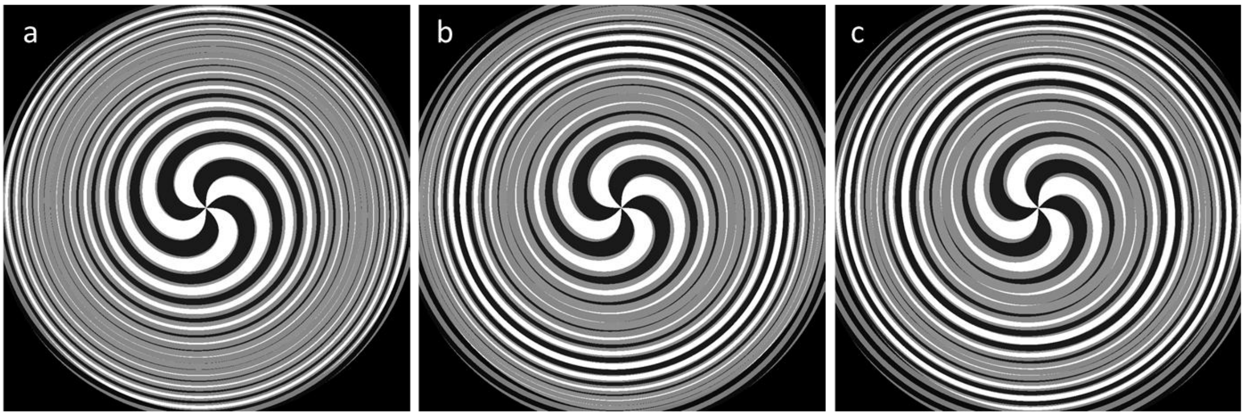

Figure S16. Overlapping of the internal structure of the 4-charge SZP pattern: unstretched one and a 4, 8 and 12% radially stretched ones, used in numerical simulations.

2.2. Evolution of the beam structure near the focal plane

Revealed heterogeneous radial variation of the stripes position may lead to the conclusion that the performance of such SZP depends on the incident beam size. But in the numerical model, we used a Gaussian beam with an 11 mm waist radius, closely matching the experimental conditions (Figure S17a). From the other side, it is known, that vortex beams undergo the azimuthal rotation of their inherent structure during the propagation [1] . Calculated intensity distributions, obtained for the diffraction on the unstretched SZP at distances z = 8 and z = 8.5 mm also verify this statement (Figure S17b, c). Two white lines depict the shift of the beam maximum during the propagation between these planes on the angle ~8°).

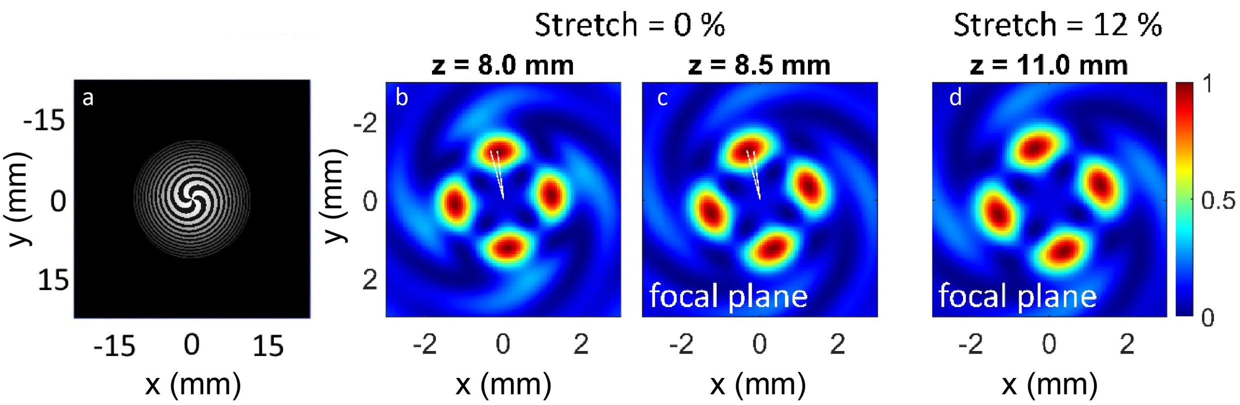

Figure S17. a) Comparison between an unstretched 4-charge SZP pattern and a 12% radially stretched one, used in numerical modelling. The pattern of unstretched SZP is shown semi-transparent. Simulated intensity distributions b) near focus at 0% SZP stretch; c) in focus at 0% SZP stretch; d) in focus at 12% SZP stretch.

On the contrary, the focal-plane intensity distributions for SZP in both the unstretched and stretched states (Figure S17c, d), respectively) show that the coordinates of the intensity maxima within the focal planes remain nearly identical, regardless of the stretch. Thus, it can be concluded that the focal planes, defined in the experiment and the simulation for various SZP stretch states, have inconsistent axial positions.

3. The principle of multiple-image wavefront retrieval with a focal-tunable device as a scan-free alternative to longitudinal detector translation

The comprehensive characterization of THz structured light fields remains impossible using only amplitude information. Retrieving the phase of these fields has become crucial for advancing applications in imaging and communications. The Single Beam Multiple Intensity Reconstruction (SBMIR) algorithm [2] is an iterative phase retrieval method implemented in a single-beam setup. Its implementation is simple, requiring only a dataset of intensities measured at various planes along the propagation axis to ensure sufficient variation in the recorded diffraction patterns. This technique has been successfully demonstrated for wavefront characterization in the THz range[3–7], including the analysis of structured light fields[7]. However, its conventional implementation requires precise mechanical scanning of a detector, making the setup complex and slow.

This section outlines the concept and advantages of employing fabricated tunable devices for phase retrieval, demonstrated here using the SBMIR algorithm**.** We introduce an alternative to conventional longitudinal scanning by mechanically varying the focal plane of a fabricated SZP[8] (Figure S18).

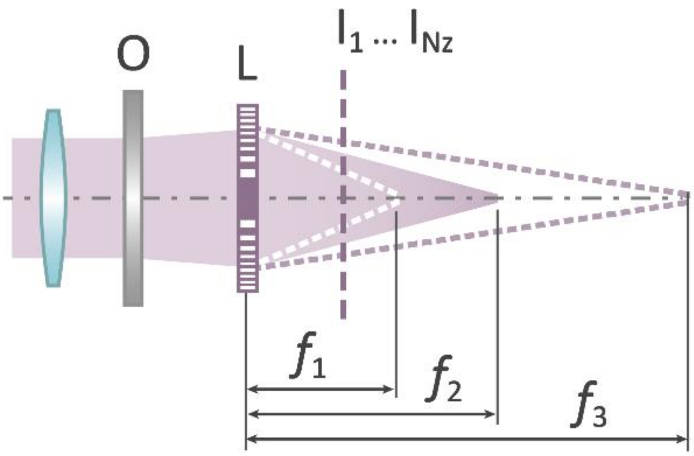

Figure S18. Schematic of the phase retrieval setup with a focal-tunable lens replacing longitudinal scanning.

This approach is functionally equivalent to the detector shifting, as the diffraction pattern observed at a fixed plane for a stretched SZP is nearly identical to the pattern from the unstretched SZP dataset at the corresponding focal-shifted plane, differing by a magnification factor. In Figure S16, a numerical examination is presented on wavefront phase retrieval conducted with a fabricated stretchable four-charge SZP at 0.327 THz. The simulation was performed using the angular spectrum of plane waves method implemented in MATLAB. The computational domain had a field of view (FOV) of 60 mm sampled with 2000 points (spatial step Δx = 30 μm, ~λ/30), which ensures adequate numerical representation of the fine structure of SZP. At a lower resolution (spatial step Δx = 450 μm, ~λ/2), which corresponds to the practical limit of the angular spectrum method, the spatial parameters of the focused beam do not have principial differences. Using a higher spatial resolution in the calculation yields smoother and more easily interpreted field distributions and allows for a more accurate consideration of the structure and position of the SZP.

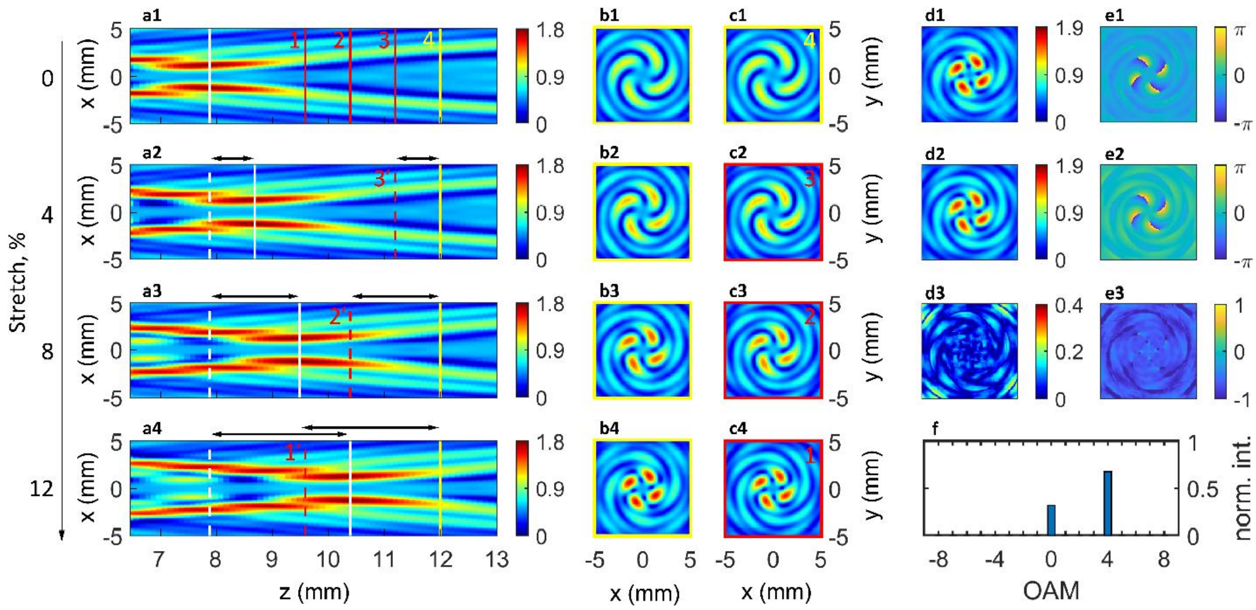

Figure S19. Numerical examination of phase retrieval with a stretch-tunable SZP based on SWCNT film at a 0.327 THz. (a1-a4) Longitudinal cross-sections of the simulated field amplitude (6.5-13 mm behind the SZP) at 0%, 4%, 8%, and 12% mechanical stretch. Amplitude distributions at (b1-b4) the z = 12 mm plane (yellow line) for different SZP stretch levels, and at (c1-c4) the planes corresponding to positions 1-4 in the 0%-stretch SZP dataset. (d1, d2) Amplitude and (e1, e2) phase reconstructed using the datasets in (b) and (c), respectively. (d3, e3) Corresponding amplitude and phase difference maps, (f) OAM spectrum.

Column (a) of Figure S19 shows simulated longitudinal distributions of the amplitude from 6.5 to 13 mm formed behind the SZP under mechanical stretch levels from 0% to 12%. The focal plane is marked by a solid white line, and a dashed white line shows its position for the field distribution formed by the unstretched SZP. The focal distance increases from 7.9 mm to 10.4 mm over 0-12% SZP stretch, shifting by ~0.8 mm per 4% stretch (focal distances defined here show a slight variance from those reported in the main manuscript). The fixed plane at z = 12 mm, indicated by the yellow line, represents the detector location where amplitude distributions are assumed to be recorded for each SZP state. The resulting amplitude patterns are shown in Figure S19(b1-b4). Using the calculated focal plane shift, equivalent patterns (Figure S19(c1-c4)) were identified in the unstretched SZP dataset. Their positions are marked by solid red lines in the longitudinal distribution of Figure S19(a1). The dashed red lines in Figure S19(a2-a4) point to the specific plane in the (a1) distribution that contains a field pattern equivalent to the one observed at the fixed yellow plane for each SZP stretch state.

Figure S19 (d1,d2) and (e1,e2) show the amplitude and phase, respectively, retrieved from the diffraction patterns in columns (b) and (c). The corresponding difference maps for amplitude and phase are shown in panels (d3) and (e3). These difference maps reveal a discrepancy between the two reconstructions, which originate from a minor larger beam profile observed during SZP stretching. For experimental purposes, this discrepancy is negligible compared to the typical variances introduced by a non-Gaussian beam profile or an imperfect focal plane shift measurement. Despite this, the numerical experiment confirms the implementation of SBMIR with focal-varying approach successfully reconstructs a phase profile that identifies the four-charge beam. Figure S19(f) presents the OAM spectrum, revealing topological charges of orders 4 and 0 with relative intensities of 0.7 and 0.3, respectively, as determined from the retrieved complex amplitude following the approach in [7].

References

1. Petrov, N. V, Pavlov, P. V & Malov, A. N. Numerical simulation of optical vortex propagation and reflection by the methods of scalar diffraction theory. *Quantum Elec (Woodbury)* **43**, (2013).
2. Pedrini, G., Osten, W. & Zhang, Y. Wave-front reconstruction from a sequence of interferograms recorded at different planes. *Opt Lett* **30**, (2005).
3. Petrov, N. V. *et al.* Terahertz Multiple-Plane Phase Retrieval. in *Imaging and Applied Optics Congress* HF4G.8 (Optica Publishing Group, Washington, D.C., 2020). doi:10.1364/DH.2020.HF4G.8.

4. Petrov, N. V. *et al.* Terahertz phase retrieval imaging in reflection. *Opt Lett* **45**, (2020).

5. Agour, M. *et al.* Chocolate inspection by means of phase-contrast imaging using multiple-plane terahertz phase retrieval. *Opt Lett* **47**, (2022).

6. Chopard, A. *et al.* Single-scan multiplane phase retrieval with a radiation of terahertz quantum cascade laser. *Appl Phys B* **128**, (2022).

7. Radivon, A. V. *et al.* Expanding THz Vortex Generation Functionality with Advanced Spiral Zone Plates Based on Single-Walled Carbon Nanotube Films. *Adv Opt Mater* **12**, (2024).

8. Mosso, F., Peters, E. & Pérez, D. G. Complex wavefront reconstruction from multiple-image planes produced by a focus tunable lens. *Opt Lett* **40**, (2015).